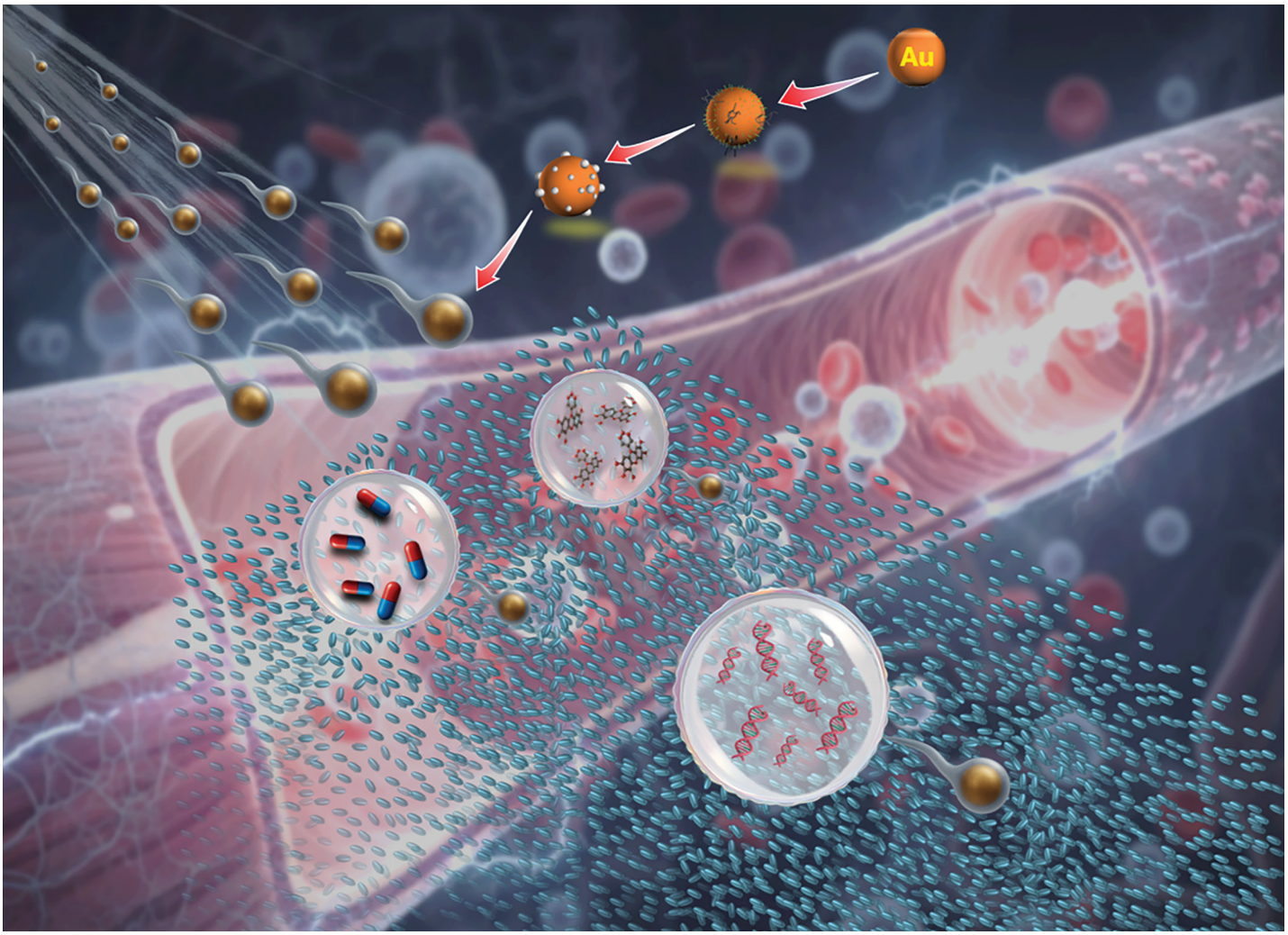

Showcasing research from Professor Xiao Li's laboratory, Department of Materials Science & Engineering, University of North Texas, Denton, USA.

Asymmetry-driven irregular topological defects and hydrodynamic cavitation of tadpole particles in nematic liquid crystals

Asymmetric tadpole-shaped Janus nanoparticles with gold cores and flexible silica tails were synthesized. The micrometer-sized SiO_2 tails exhibit exceptional flexibility, distorting the surrounding liquid crystal (LC) field into butterfly-shaped topological defects. As these particles moved through the LC medium under capillary forces, dynamic interfacial fluctuations between the air and LC phases facilitated the formation of metastable cavities under a balance among capillary, elastic, and viscous forces. These findings advance fundamental understanding of defect–fluid interactions and offer potential applications in microactuators, adaptive optics and targeted drug delivery.

Image reproduced by permission of Xiao Li from *Mater. Adv.*, 2025, **6**, 6711. Image generated by Google Gemini.

As featured in:

See Ying Bao, Xiao Li *et al.*, *Mater. Adv.*, 2025, **6**, 6711.

ROYAL SOCIETY OF CHEMISTRY

rsc.li/materials-advances

Registered charity number: 207890

Materials Advances

ROYAL SOCIETY OF CHEMISTRY

PAPER

View Article Online
View Journal | View Issue

Cite this: *Mater. Adv.*, 2025, **6**, 6711

Asymmetry-driven irregular topological defects and hydrodynamic cavitation of tadpole particles in nematic liquid crystals

Xiaowei Wang,†[a] Teagan Hamlett,†[b] Sid Hashemi,[a] Joseph E. Doebler,[b] Tasha Joy,[a] Giordano Tierra,[c] Ying Bao*[b] and Xiao Li*[a]

Topological defects (TDs) arise from the disruption of orientations that span multiple length scales, from nanometers in biological systems to miles in cosmic systems, often resulting from energy minimization leading to symmetric morphologies. Symmetry breaking is a challenge in creating new types of topological defects to understand self-assembly mechanisms when driving the system away from the equilibrium state. Nematic liquid crystals (LCs) provide an ideal system to create, annulate, and directly visualize TDs. We use asymmetric particles, named tadpole-shaped particles, which have sphere-shaped heads and long tails, to explore new symmetry-breaking defect morphologies when dispersing these tadpole particles into nematic liquid crystals. Experimental observations and numerical simulations demonstrated that the micrometer-sized SiO_2 tails exhibit exceptional flexibility, distorting the surrounding LC field into butterfly-shaped defects. As these particles moved through the LC medium under capillary forces, dynamic interfacial fluctuations between the air and LC phases facilitated the formation of metastable cavities. This novel system enabled cavity generation and revealed a unique formation mechanism driven by hydrodynamic cavitation, where a balance between capillary, elastic, and viscous forces led to cavity contraction and equilibrium restoration. Beyond advancing fundamental understanding, these findings open new avenues for designing microactuators, soft robotics, and adaptive materials, transforming the role of active particles in LC systems.

Received 27th May 2025,
Accepted 3rd August 2025

DOI: 10.1039/d5ma00550g

rsc.li/materials-advances

Introduction

Topological defects, perceived as disruptions in uniform fields, have attracted extensive interest across condensed matter physics,[1] cosmology,[2] and biological systems.[3] In soft condensed matter, topological defects influence phase transitions and material properties,[4] such as affecting viscoelasticity in biological polymers and proteins,[5] exhibiting skyrmions with unique vortex structures in superfluid ferromagnetic spinor condensate,[6] and enabling autonomous motion in active materials.[7] Liquid crystals (LCs), due to their molecular anisotropy and intermediate fluid–solid characteristics, provide an ideal environment to investigate defect formation and evolution.[8–12] In particular, by introducing colloidal particles into nematic LCs that only have orientational order, topological defects can be generated and further controlled through the boundary conditions imposed by the particle surfaces on the LC director fields.[13–16] Spherical microparticles with homeotropic anchoring form dipolar configurations with hyperbolic hedgehog defects, whereas planar anchoring creates quadrupolar Saturn-ring defects.[17–19] These defect complexes behave analogously to electrostatic monopoles, dipoles, or quadrupoles, driving elastic interactions to facilitate colloidal self-assembly.[20,21] Defect morphology is also highly dependent on particle geometry: spherical particles produce Saturn rings or boojum-type defects,[22] rods induce disclinations and dislocations,[17,23] and ellipsoids yield dipolar and quadrupolar defects. Furthermore, breaking the particle's symmetry leads to more complex distortions and induces a multitude of possible defect configurations in the surrounding liquid crystal. The Janus particle surface has two distinct physical properties that can generate an asymmetric LC director field, which induces a controllable propulsion behavior, with the velocity strongly influenced by electric polarizability.[24] A recent study has shown that even slight anisotropy in particle shape can lead to defect polymorphism, where either point or ring defects may nucleate at different locations on the particle depending on its

[a] *Materials Science and Engineering Department, University of North Texas, Denton, TX, 76207, USA. E-mail: Xiao.Li@unt.edu*
[b] *Department of Chemistry, Western Washington University, Bellingham, WA, 98226, USA. E-mail: Baoy@wwu.edu*
[c] *Department of Mathematics, University of North Texas, 1155 Union Circle, Denton, TX, 76203, USA*
† These authors contributed equally.

orientation and interactions, in contrast to the unique defect type imposed by a symmetric particle.[25] Diverse defect morphologies and rich behaviors suggest that particle asymmetry provides a new approach to tune topological defect arrangements in LCs.

Inspired by motile microorganisms in nature, bacteria and spermatozoa possess an asymmetric head–tail geometry to interact with their surrounding environments, which is crucial for propulsion in fluids by breaking temporal symmetries of motion.[26] Such self-propelled mechanism of microorganisms results in complex, time-dependent defect configurations that are typically not replicated by passive particles.[27–29] Therefore, synthetic particles with integrated asymmetric geometry and composition are developed to mimic the biological active particles and are expected to outperform microorganisms in more complex or harsh environments. For example, snowman-shaped particles show defect polymorphism, leading to the formation of various defects influenced by the asymmetry of particle shape, thus affecting their electrophoretic behavior under an electric field.[25] More importantly, the resulting asymmetric director field and the subsequent self-propulsion or externally stimulated propulsion behavior also attract a lot of research interest due to the controllable motion of particles. The propulsion velocity of Janus particles is closely linked to their electric polarizability.[24] On the other hand, the dynamic flows usually considered in such biological systems play a crucial role in various physiological processes and can enable vapor nucleation in liquids. This hydrodynamic cavitation forms transient cavities or vapor bubbles in the liquid when the local pressure drops below the vapor pressure. It has been well-studied in conventional (isotropic) liquids and is known for its role in processes of biomedical ultrasound.[30–33] However, cavitation in anisotropic liquids is rarely explored due to the complexity of ordered fluids. Recently, a micropillar was created at the center of a microfluidic channel of nematic LCs to induce negative pressure by changing the flow rate, thereby forming a cavity behind the micropillar.[34] To date, the study of cavitation in anisotropic liquids, especially in liquid crystals, is limited and still mainly focuses on phase transitions under negative pressure.[35]

In this work, by leveraging the unique defect structures and motion behaviors that arise from asymmetry, we aim to explore the influence of asymmetry-driven morphology on the formation of topological defects in nematic LCs using the synthesized tadpole-shaped nanoparticles. Relying on the synthetic gold nanoparticles (GNPs) coated with silica shells with Janus tadpole-like structures (JT-GNPs), the silica tadpole tail length can grow to micro size on gold cores with various diameters. By mixing the JT-GNPs with nematic LCs, we investigated how the asymmetric properties of JT-GNPs can affect the formation of irregular defect morphologies, such as butterfly-like defects in this system. The effect of different boundary anchoring conditions on these defect morphologies is systematically analyzed using planar, weak, and strong homeotropic anchoring. In particular, the flexibility of the long SiO_2 tail is examined for the first time to understand its contribution to hydrodynamic cavitation and cavity formation. Furthermore, the interplay between hydrodynamic fluids and dynamic defect behavior on the cavity formation mechanism is revealed, and how the cavity size is affected by the JT-GNP characteristics, such as size and travel distance through the LC medium, is further explored. The simulation is also performed to study the director field deformation surrounding JT-GNPs associated with the proximity of the JT-GNPs to the cavities. These findings offer valuable insights into potential applications, such as tuning defect structures for microactuators, soft robotics, and adaptive materials, by precisely controlling particle-induced distortions.[36]

Results

Janus tadpole morphology particles to create irregular shaped topological defects in nematic LCs

GNPs coated with silica nanoshells with Janus tadpole morphology, named JT-GNPs, were synthesized by modifying the ligand ratio and system pH. The schematic in Fig. 1a illustrates the process of fabricating JT-GNPs and detailed synthesis information is provided in the SI. To reveal the effect of the asymmetric geometry of JT-GNPs on the topological defect morphology of LCs, the 5CB LC was mixed with JT-GNPs as shown in Fig. 1b. LC cells were created with different boundary conditions. The top glass surface of the cell was cleaned with Piranha solution and modified with octadecyl–trichlorosilane (OTS) to provide strong homeotropic anchoring. The bottom substrate anchoring orientation and strength toward LCs were varied as follows: a Piranha-cleaned Si surface to provide planar anchoring, and a self-assembled monolayer of hydroxyl-terminated poly(6-(4-methoxy azobenzene-4′-oxy)hexyl methacrylate) (PMMAZO) to provide tunable homeotropic anchoring by varying the grafting density of the brush layer (a PMMAZO example is shown in Fig. 1c). According to our previous work,[37] the brush layers were formed by coating PMMAZO with two different thicknesses onto a cleaned Si wafer and annealing at 250 °C for 5 mins. The resulting grafting density of the PMMAZO brush was controlled to be $\sim$0.02 chain per nm^2 and $\sim$0.06 chain per nm^2, depending on the film thickness, to induce perpendicular and tilted orientations of the affiliated LCs, respectively. The LC cell was fabricated following the process in Fig. 1c: the OTS-modified glass as top plates and PMMAZO-coated Si substrate as the bottom were assembled face-to-face with a plastic spacer to control cell thickness. LCs and JT-GNPs were uniformly mixed as a solution (Fig. 1d) and injected into this hybrid LC cell through capillary action. As shown in Fig. 1d, the fluorescence optical image indicated that by dispersing JT-GNPs in a viscous solution (clear nail polish solution) similar to LCs, the long tail could fully extend in the viscous solution, and particles could be characterized as individual particles without entanglement of long tails. This was crucial for subsequent characterization of the LC cell to isolate particles for defect structure analysis. The surface anchoring of JT-GNPs was considered planar due to the characteristics of the

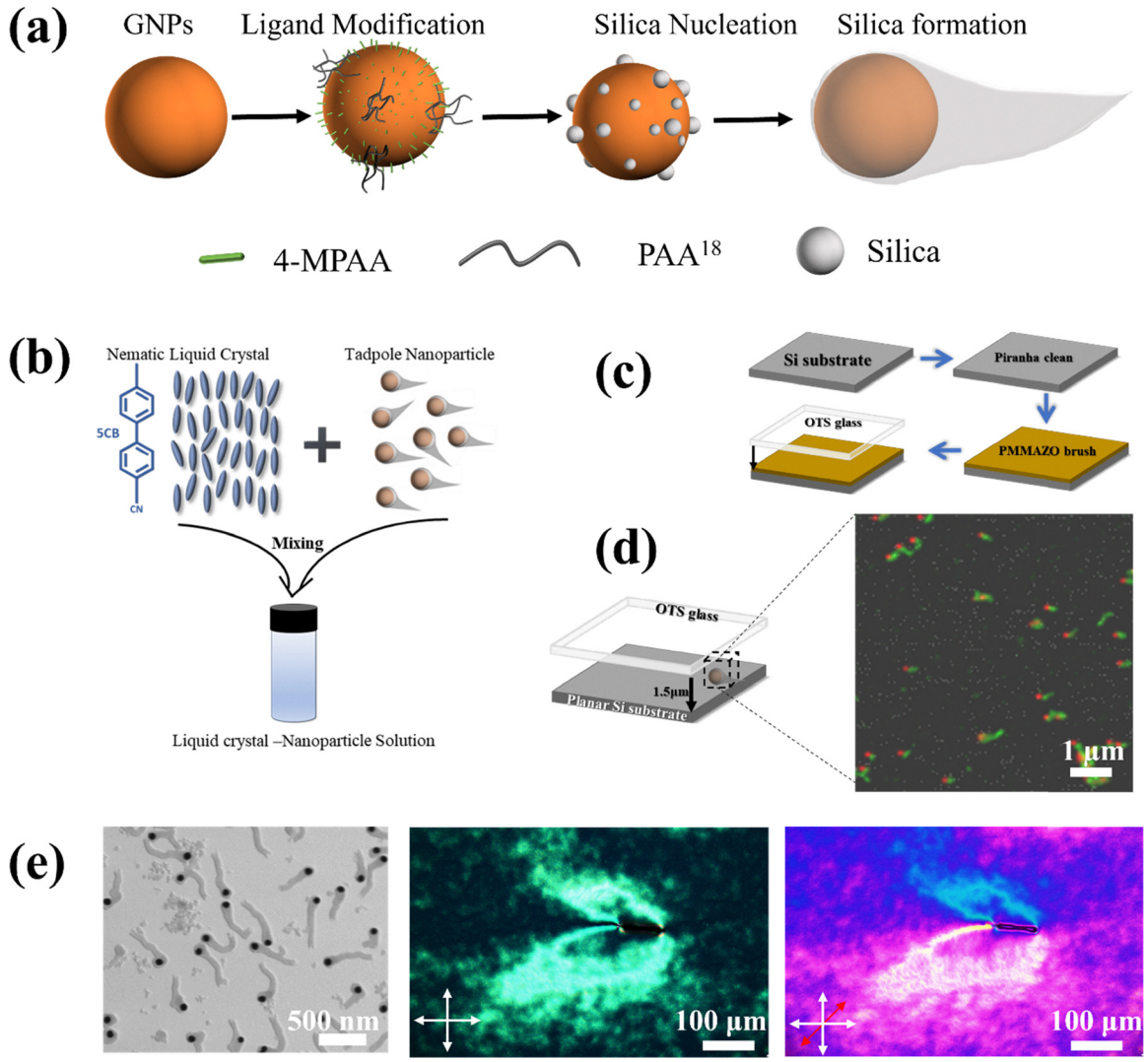

Fig. 1 Synthesis and characterization of the Au–SiO_2 Janus tadpoles (JT-GNPs). (a) Schematic illustration of the formation of the JT-GNPs. (b) Schematic illustration of the preparation process for the 5CB and JT-GNP solution. (c) Diagram depicting the assembly of LC cells with PMMAZO surface anchoring conditions. (d) Fluorescence microscopy image of FITC-conjugated JT-GNPs. (e) STEM image of JT-GNPs (left); polarized Optical Microscopy (POM) image of the JT-GNP/5CB solution (middle); retardation image using a 530 nm wavelength filter (right).

coated SiO_2. The director field of the LC and JT-GNP mixture was characterized using polarized light microscopy and analyzed based on the observation of the birefringence phenomenon. As shown in Fig. 1e, the STEM image of the test JT-GNPs showed that the gold sphere head was 70 nm in diameter and the SiO_2 tail was around 700–800 nm. An irregular 'butterfly' morphological defect was generated by JT-GNPs. The orthogonal polarized image indicated a −1 defect formed from the sphere-shaped head of the JT-GNPs; the branched schlieren line defect connected toward the narrowed cavity, which was induced by the long SiO_2 tail fluctuation in LCs. By using a first-order retardation plate (λ = 530 nm) to convert the director orientations with color differences, the two butterfly wings appeared magenta and blue, corresponding to the director being parallel or perpendicular to either the polarizers or the slow axis of the retardation plate.

Topological defect morphology changes with the confined boundary anchoring conditions

To investigate the influence of nanoparticle morphology on the orientation of LCs and subsequent air cavity formation, two types of GNPs with the same core size but different tail lengths were used, as shown in Fig. 2(b and c). These nanoparticles were chosen with a core diameter of 110 nm; one variant exhibited tail lengths ranging from 1000 to 1500 nm, whereas the other variant had shorter tails ranging between 400 and 700 nm. By maintaining a consistent core diameter and altering only the tail length, our study meticulously isolated the effect of tail dimension variations on the director field configurations of LCs. Further dimensions of our study involved the exploration of different surface anchoring conditions: planar, weak homeotropic, and strong homeotropic surface anchoring. The modulation between weak and strong homeotropic conditions was achieved

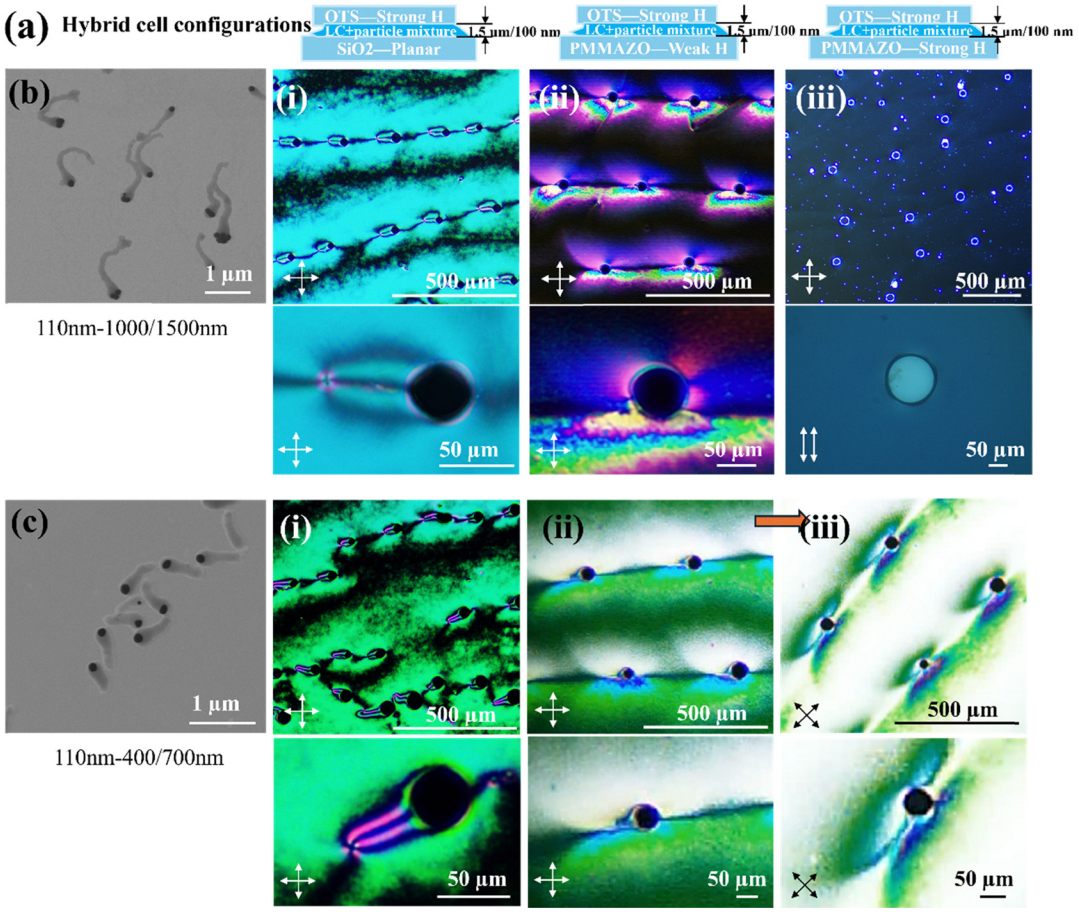

Fig. 2 Surface morphology of JT-GNPs under different surface anchoring conditions. (a) Schematic representation of LC cell configurations: planar anchoring substrate, PMMAZO-induced weak homeotropic anchoring substrate, and PMMAZO-induced strong homeotropic anchoring substrate (from left to right). In all configurations, the top surfaces exhibit strong homeotropic anchoring. (b) JT-GNPs with a core diameter of 110 nm and a tail length ranging from 1000 to 1500 nm. (i)–(iii) represent JT-GNPs under various LC cell configurations as outlined in (a). (c) JT-GNPs with a core diameter of 110 nm and a tail length ranging from 400 to 700 nm under two different cell configurations (i) and (ii).

by adjusting the concentrations of PMMAZO. All samples displayed cavities despite the different morphologies. In the homotropic-planar cell, for both JT-GNP-110-1000/1500 nm and JT-GNP-110-400/700 nm GNPs, the small dark nucleus surrounded by a faint concentric ring on the left was a JT-GNP. On the right, the dark circle represented a cavity generated by the JT-GNP. The JT-GNP, with its distinctive elongated tail, created a directional impact that manifested as a dark streak extending from the nanoparticle towards the cavity. This dark streak represented a linear defect where the LC molecules exhibited discontinuous alignment. From both the top and the bottom of the JT-GNP, two additional defect lines converged towards the cavity. These dark lines suggested the presence of topological defects, which are common in LCs subjected to constrained geometries or varying boundary conditions. The JT-GNP with a 110 nm diameter core and a 1000–1500 nm tail exhibited a wider disclination line defect compared to the JT-GNP with a 110 nm diameter core and a 400–700 nm tail. The longer tail likely induced a more significant perturbation in the surrounding medium, affecting the LC director field. Under planar–homeotropic conditions, the particle swam further from the cavity compared to the homeotropic–homeotropic case, due to reduced surface roughness and minimal entanglement with the bare SiO_2 surface. This allowed the particle to create a cavity and still travel a certain distance from it. Under planar-strong homeotropic conditions, the JT-GNP swam further from the cavity due to reduced surface roughness and minimal entanglement with the SiO_2 surface, leading to greater perturbation in the surrounding LC director field. Under strong–weak homeotropic boundary conditions in Fig. 2b(ii), a butterfly-like defect formed around the cavity for both sizes of GNPs. Two wing-like regions with different colors were observed above and below the cavity, indicating different LC molecular alignments. The JT-GNP was observed to be positioned very close to the cavity, and the +1 defect was located at the position of the JT-GNP, with two disclination lines extending from the +1 defect core, forming a wing-shaped defect around the cavity. Unlike the strong homeotropic–planar cell, the distance between the JT-GNP and the cavity was very small.

This was similar to what happened in the strong homeotropic–strong homeotropic cell configuration (Fig. 2a(iii)), where the JT-GNP and the cavity were almost in contact, initially generating a butterfly defect and cavity due to the strong

capillary force directing the particle's movement. However, as the strong homeotropic anchoring dominated, all LC molecules aligned perpendicularly to the surfaces, erasing the defect features. Despite this, the air–LC interface surrounding the cavity retained a bright circular appearance. Since both the top glass and Si substrate had strong homeotropic surface anchoring, 5CB molecules aligned perpendicularly to the surface under boundary constraints, and the observed defect feature (Video S1) vanished rapidly as the capillary flow stopped and the boundary condition dominated the anchoring. Due to the existence of the tail and its fluctuation when the mixed solution flowed into the cell, each JT-GNP still generated a cavity. Variations in tail length induced different perturbations in the surrounding regions, leading to local density changes, which in turn triggered the nucleation of cavities. From experiment, variations in cavity size were consistently observed for particles with different tail lengths under various anchoring conditions. For instance, in the case of a 110 nm diameter core with a tail length of either 1000–1500 nm or 400–700 nm, the longer tail (1000–1500 nm) formed larger cavities in both the strong homeotropic–planar and strong–weak homeotropic cell configurations. Furthermore, for the longer tails (1000–1500 nm), with the surface anchoring strength transitioned from planar to weak homeotropic, the cavity size increased with average sizes of approximately 45 μm and 55 μm. In contrast, shorter tails (400–700 nm) showed relatively smaller cavity sizes with average sizes consistently ranging from approximately 40 μm to 50 μm, also showing dependence on the anchoring conditions. However, this effect did not occur for spherical particles, as shown in Fig. S1, where no cavity was formed. This suggested that the shorter tail had a minimal effect on cavity formation, whereas spherical particles did not form cavities due to the absence of asymmetrical tails.

Moreover, a bright circle was visible around each cavity in Fig. 2. The cavity acted as an isotropic cavity within the nematic host. Due to the homeotropic boundary condition at the cavity–LC interface, the 5CB molecules around the cavity were forced to reorient in a radial manner, generating a spherically symmetric configuration around the cavity. This radial alignment around the cavity introduced elastic distortion to the surrounding LC due to the deviation of the director field from the far-field uniform homeotropic state. The bright circle observed around the air cavity under crossed polarizers could be attributed to the anisotropic refractive index distribution generated by the deformation of the nematic director field. Under crossed polarizers, the birefringence of the 5CB caused an optical path difference, which produced interference patterns that appeared as bright regions. The bright circle around the cavity represented the spatial variation of the birefringence caused by the radial orientation of the LC molecules, which created areas of different optical retardation when the polarized light passed through regions with different director orientations.

Hydrodynamic cavitation induced by flexible SiO_2 tail fluctuation in anisotropic media

The dynamic interaction between JT-GNP and 5CB provided important insights into the mechanisms governing cavity formation and particle behavior in fluids when the JT-GNP and 5CB mixed solution was injected into a cell with a strong–weak homeotropic anchoring configuration. To ensure uniform injection, the solution was slowly administered at a rate of approximately 0.15 μL per second. After injection, the solution dispersed in all directions due to capillary forces between the glass and the Si substrate, as illustrated in Fig. 3a and b. We chose to focus our study on the middle region of the cell to ensure the homogeneity of the cavities without distortion due to side effects such as directional variation or edge effects of the cell. As shown in Fig. 3b, the lines formed by the cavities intersected and were unevenly distributed when close to the cell edge. In Fig. S2, the cavities formed near the cell edge were distorted, exhibiting random sizes and shapes, likely due to inconsistencies in the initial injection force, such as variations in injection velocity and uneven flow dynamics near the cell boundaries, which caused disruptions in multiple directions. Additionally, the proximity to the edge resulted in altered capillary forces, contributing to irregular cavity shapes and sizes.

As the JT-GNP and LCs mixed solution moved forward under the action of capillary force, multiple concave pits were generated at the solution–air interface. In each concave pit, it was speculated that one JT-GNP became trapped with no visible cavity at the beginning, as shown in Fig. 3d at 0 seconds. At this moment, the fluctuation from the JT-GNP's long tail began to disturb the local LC director field and further split the solution at the front air interface at 0.5 seconds. By 0.7 seconds of forward flow, the separated solution reunited and enclosed the air to form a cavity. Whenever JT-GNPs appeared at the pits, the solution split, recombined, and enclosed the air again at the front solution–air interface. Following the capillary force direction, the JT-GNPs aligned along with the injection direction, and due to the deformation of the LC director field around the tail, a color difference was generated along the concave edges. The deformation of the LC continued to grow, and the surrounding molecules underwent significant reorientation to accommodate the growing cavity. The cavity became larger and more sharply defined, with a distinct black boundary between the encapsulated air and the surrounding LCs. The 5CB molecules experienced different alignments due to the localized stress and flow dynamics induced by the movement of the JT-GNP. The realignment of LCs surrounding the cavity formed a stable structure in which the cavity maintained its shape and was characterized by the absence of LCs in that region. Video S2 provides a more detailed cavity formation process. This formation of cavities in anisotropic liquids has only been demonstrated in microfluidic systems, where a sudden pressure drop occurred when LC flow passed a cylindrical obstacle within a microchannel, creating a cavity domain behind the obstacle.[34] In this study, the JT-GNP caused significant perturbations in the nematic 5CB, leading to a local sudden drop in pressure as the particle moved forward, which in turn resulted in cavity nucleation.

As the JT-GNP moved away from the injection area, the cavities formed behind the particles became smaller. Fig. 3e illustrates the distinct pattern formed by the movement of

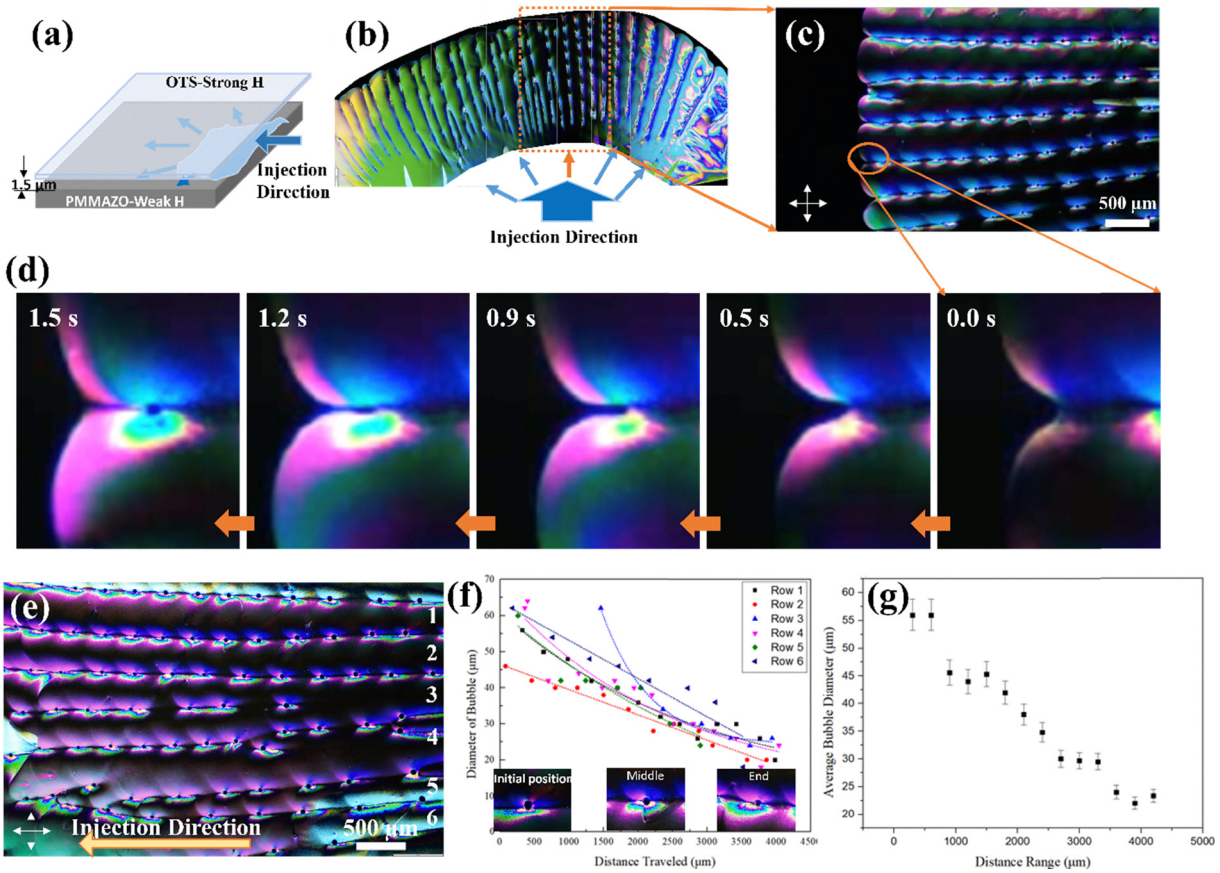

Fig. 3 Formation and migration trajectories of cavities induced by JT-GNPs. (a) Schematic representation of the flow direction during the initial injection process. (b) Observation of solution flow diverging in various directions, with the central region exhibiting more uniform cavity formation. (c) Formation of cavities as the solution flows from right to left. (d) Detailed view of cavity formation dynamics. (e) Morphology of cavities post-injection. (f) Relationship between cavity diameter and the distance traveled by each formed cavity. (g) Correlation between average cavity diameter and the distance traveled by the cavities.

JT-GNP in the LC solution. As the nanoparticles moved, they left behind a trail of cavities that were aligned into a defined linear pattern. The cavities were larger and more widely spaced when the distance traveled from the initial injection area was shorter, but the cavity size decreased as the particles moved further along their path. As shown in Fig. 3(f and g), the diameters of the cavities were measured for each row, indicating that the cavity size decreased with distance from the initial injection area. Additionally, the distance between each cavity decreased as the nanoparticles moved forward. This trend suggested that the conditions for cavity formation changed dynamically during the movement of JT-GNPs, which could be attributed to the reduction of capillary forces along the JT-GNP path. Initially, injection and capillary forces drove the solution flow and were sufficient to maintain the formation of large cavities. As the nanoparticles continued to move, these forces gradually decreased, making it more difficult to maintain large cavities. Consequently, smaller cavities were formed with less spacing between them, reflecting the reduction in capillary force, which led to changes in flow velocity and ultimately resulted in smaller cavities and a decrease in the distance between cavities.

Local cavitation domain shrinks according to Ericksen number

Fig. 4 shows a series of micrographs that capture the evolution of a cavity behind a JT-GNP suspended in LCs within a strong-weak homeotropic anchoring cell configuration. Fig. 4(a–c) depict the state of the cavity immediately after injection and after 3 and 6 hours, respectively, as well as the corresponding retardation images at 530 nm. The sequence revealed that over time, the cavity gradually decreased in size until it was filled with the LCs again. Due to the balance between elastic forces and the reduction of viscous stress after the flow stabilized, the LC gradually filled the cavity. The contraction of the cavity indicated that the pressure behind the particle was recovering, the elastic forces became dominant, promoting equilibrium, and minimizing the interfacial area. By 6 hours (Fig. 4c), the cavity had been filled with LCs. Fig. 4d and e further illustrated the evolution of the cavities over a large area, providing a broader perspective on the dynamic process of cavity formation and disappearance, highlighting the uniformity achieved in the LC environment as the cavities were filled over time.

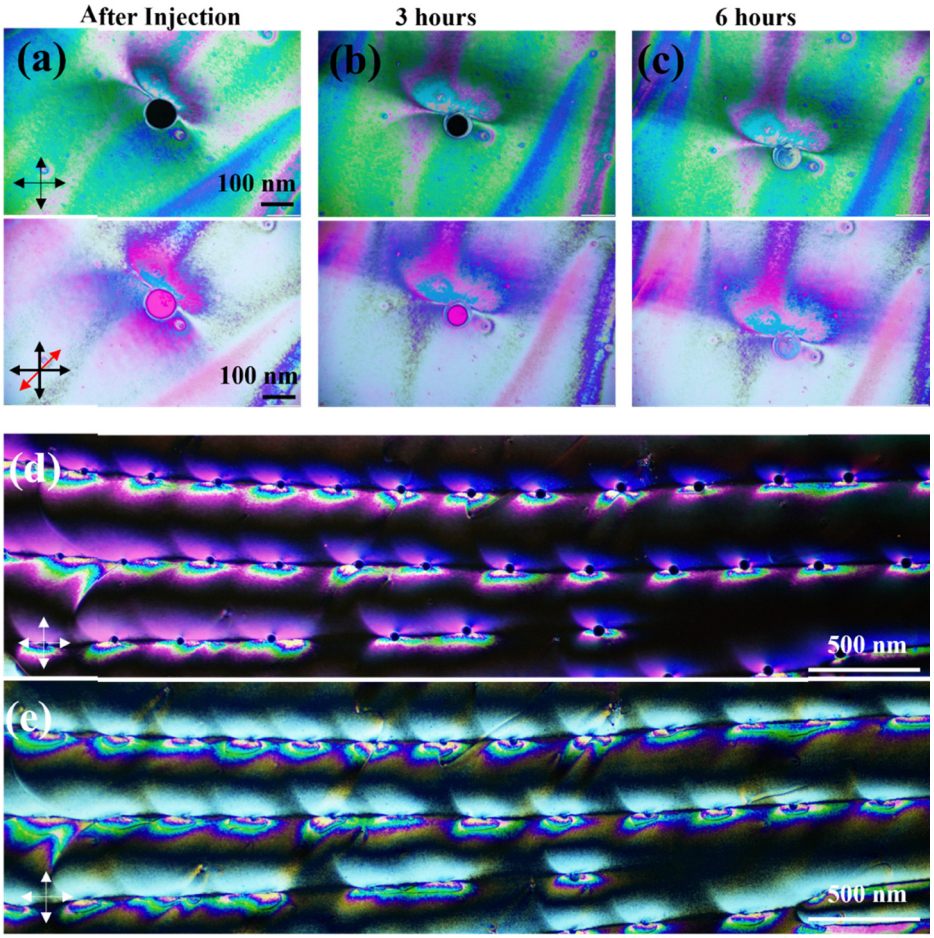

Fig. 4 Evolution of cavity shrinkage over time. (a) Cavity immediately post-injection; (b) progressive cavity shrinkage observed after 3 hours; (c) further reduction in cavity size after 6 hours with retardation observed using the UTP530 nm filter. (d) POM image illustrating the overall cavity distribution within the solution shortly after injection. (e) Complete disappearance of cavities observed after 6 hours.

Discussion

The flexibility of the thin silica tail has been evaluated through fluorescein isothiocyanate (FITC) molecules, which were encapsulated within the silica shell to provide enhanced and sustained fluorescence.[38,39] To observe individual particles, JT-GNPs with a 300 nm GNP core and ~1500 nm tail were used (a representative STEM image is shown in Fig. S3). To synthesize the FITC-conjugated silica shell, an (3-aminopropyl)trimethoxysilane (APTMS)-modified silica shell was first synthesized, rendering NH_2 groups on the surface of the silica shell. With NH2 groups, the FITC conjugated with APTMS *via* a thiourea bond, and the silica shell was linked with FITC.[40] Clear nail polish solution was added to the FITC-conjugated JT-GNPs to increase viscosity and thus slow down the Brownian motion of the particles. Fig. 5a shows the fluorescent image of FITC-conjugated JT-GNPs. The red color is from the GNP core, and the green color is the fluorescence from the FITC-conjugated silica tail. It can be clearly observed that there are individual JT-GNPs as well as aggregated ones. To observe the movement, a short video was recorded, which can be seen in Video S3. Time series of three representative individual JT-GNPs (indicated by the yellow dashed box in Fig. 5a) are shown in Fig. 5b, illustrating the movement of silica tails. Instead of a rigid tail, the silica exhibits dynamic bending motions, as shown in Fig. 5b: at 0 s (tail straightened), at 1.5 s and 3 s (tail visibly bent), and at 4.5 s (tail returns to an extended, straight configuration). The silica tail appeared very soft and flexible and underwent free movement in the solution. It has been proven in previous work that the silica shell at the nanoscale is flexible and has much better mechanical properties, which agrees with our findings.[41–43] For example, in our previous study, a 20 nm thick silica shell covering a gold nanostructure was pushed outward during silver deposition without breaking, confirming that the silica shell has certain flexibility, consistent with our current results.[44] The softness and flexibility of the thin SiO_2 enabled the JT-GNP tail to fluctuate in the surrounding LC medium, thus creating cavities during particle movement. Our future work aims to investigate the degree of silica tail flexibility in greater detail, particularly its correlation with cavity formation during particle movement as a result of tail fluctuation.

To reveal the director field deformation surrounding the JT-GNP and its associated cavity, simulations were performed

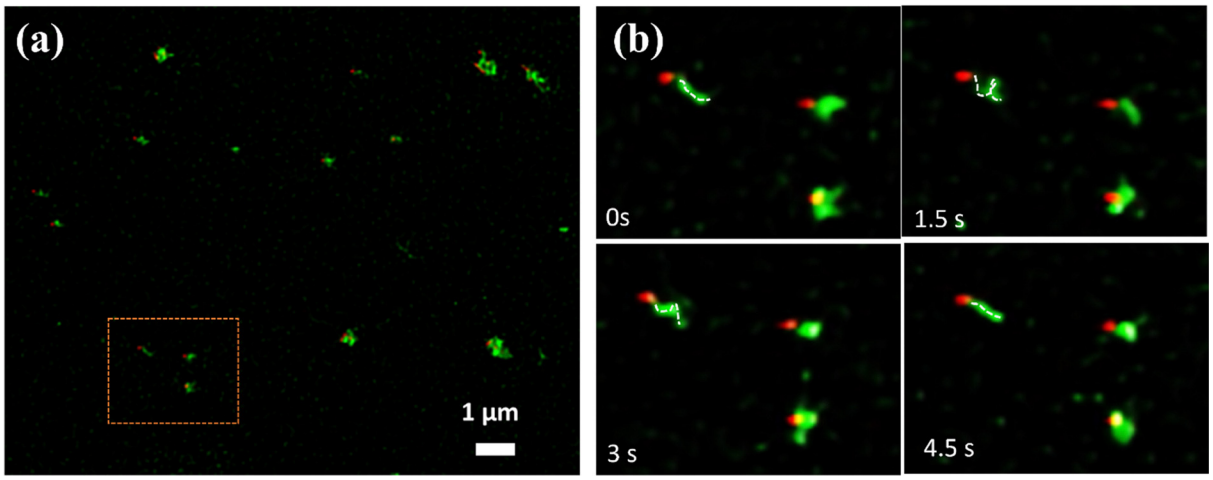

Fig. 5 Fluorescence based study on silica shell flexibility. (a) Fluorescence image of FITC conjugated JT-GNPs (300 nm core with ~1500 nm tail). The red is GNPs, green is the florescence from FITC conjugated with silica. Yellow dashed box indicates the individual TJ-GNPs. (b) Time series fluorescence images of JT-GNPs indicated as the yellow dashed box in (a) showing the movement of the silica tail in solution. Inset white dashed lines on the top left tadpole particle give an indication of possible tail behaviors at those times.

using the strong–strong homeotropic anchoring configuration as an example (Fig. 6a–c). The symmetric boundary anchoring at both the top and bottom surfaces in the simulation provided an equal view of the distorted director field, regardless of whether it was viewed from the top-down or from the side. In experiments, the polarized images were taken from a top-down view, while in the simulation of the 2D setup cell, the resulting director field images were taken from a side view. Three different initial conditions were set: the JT-GNP was positioned far away from, at a medium distance from, and close to the cavity, to analyze the interaction and morphology between the JT-GNP and the cavity in the LC medium.

When the JT-GNP was positioned very close to the cavity, the intensified interaction between the JT-GNP head and the cavity resulted in a clear dipolar defect structure. The homeotropic anchoring of the air–cavity interface competed with the planar anchoring of the JT-GNP head surface, thereby creating visible splay and bend deformations extending into the surrounding nematic matrix. The competing elastic distortions imposed by the differing anchoring conditions resulted in a localized

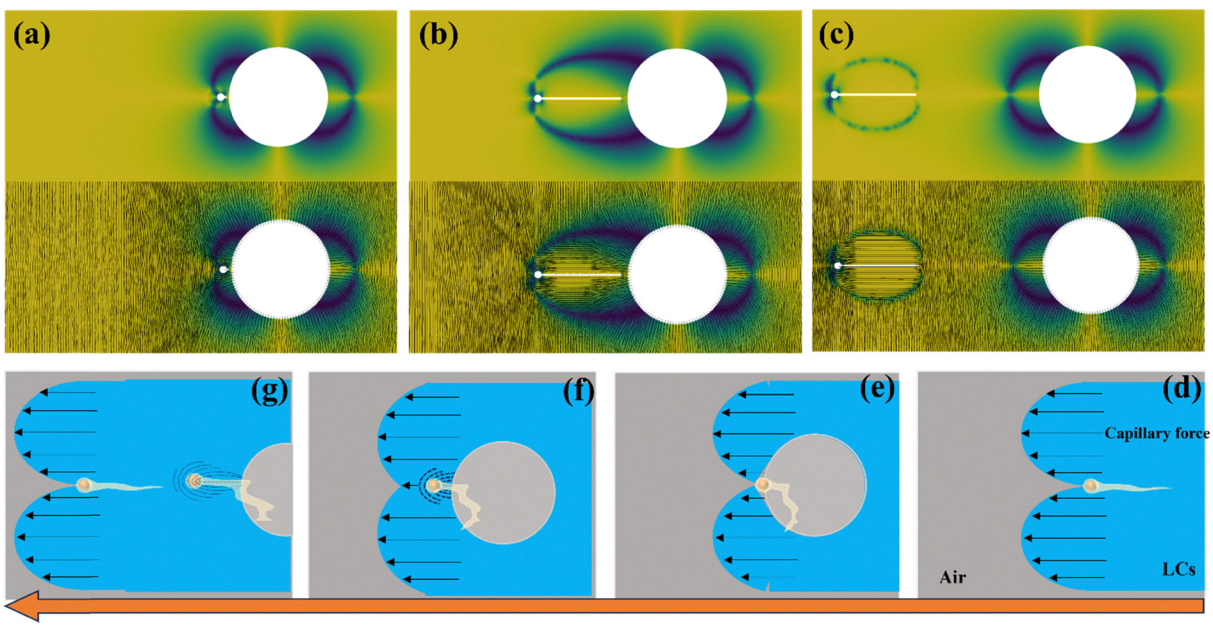

Fig. 6 Simulation results illustrating the deformed LC director field surrounding the JT-GNPs and its cavity. (a) JT-GNPs positioned near the cavity, (b) JT-GNPs at an intermediate distance from the cavity, and (c) JT-GNPs positioned far from the cavity. The small white circular with the white line represents the JT-GNPs and the large white circular represents the cavity formed by the JT-GNPs. (d)–(g) Schematic representation of the sequential stages of cavity formation when the JT-GNPs move forward in LCs.

region and disrupted the radial symmetry typically favored by the homeotropic cavity. By moving the JT-GNP further away from the cavity while still maintaining interaction, a dark defect line extended toward the cavity to compromise the anchoring difference between the planar-anchored particle surface and the homeotropic-anchored cavity interface. The distorted defect suggested that nematic elasticity mediated the interaction between the JT-GNP and the cavity, redistributing elastic stresses. This redistribution manifested as a bend toward the cavity, signifying the onset of defect coupling. The interaction at this distance showed that anchoring conditions on the JT-GNP and the cavity began to influence each other, creating a non-uniform director profile that connected the two structures. In Fig. 6c, when the JT-GNP was positioned far from the cavity, planar anchoring at the particle's head and tail resulted in a uniform director field, with nematic directors aligning parallel to the particle's surface. The visible dark defect line indicated a disclination line formed due to the mismatch in director alignment around the JT-GNP, independent of the cavity. At this distance, no significant interaction occurred between the JT-GNP and the cavity. The influence of the particle remained localized, and the cavity-induced alignment perturbations stayed distant, resulting in no coupling between the defect structures. The uniform director field highlighted the local effect of planar anchoring, with minimal distortion outside the vicinity of the particle. This suggested that elastic deformation induced by the particle was not sufficient to interact with the cavity at a distance, a situation not observed in the experiment.

Capillary forces were essential in generating the hydrodynamic force that drove the LC–air interface forward. The formation and stability of cavitation depended on the complex interplay between hydrodynamic forces, anisotropic LC properties, and interfacial dynamics. In Fig. 6d, the JT-GNP moved in the LC medium, and the particle tail caused local disturbances, resulting in capillary force at the concave point. This force created a potential energy well in which the particle was trapped, resulting in air being encapsulated behind the JT-GNP, forming an initial cavitation domain. Similar to the inception of cavitation observed in anisotropic fluids,[34] the geometry of the JT-GNP tail split the wave of the LC, thereby locally reducing the pressure, and air was drawn into the cavity. The pressure drop was crucial for the formation of the cavity. As the JT-GNP flowed further, the cavity formed and continued to expand (Fig. 6e), driven by the persistent pressure drop and the action of capillary forces. The reduction in local pressure promoted the entry of air, and the capillary force helped maintain this cavity by driving the LC–air interface forward to form an air pocket. As the JT-GNP moved further, the formed cavity reached a stable configuration (Fig. 6f). The stability of the cavity resulted from a balance between the capillary forces acting to hold the air pocket and the elastic forces of the LC resisting further deformation. The LC molecules realigned to accommodate the cavity, and the persistence of this cavitation was supported by the balance between viscous and elastic forces within LCs. This stability could be further understood through the concept of the Ericksen number.[34,45,46] When the Ericksen number fell within a specific range,[34] the coexistence of viscous and elastic effects supported the cavity's stability, preventing it from collapsing or expanding uncontrollably. This behavior was consistent with experimental observations in anisotropic liquids (Fig. 3), where stable cavitation was achieved under flow conditions that balanced these competing forces. Finally, Fig. 6g depicted a second JT-GNP entering the flow, which initiated new disturbances along the existing cavity. This introduced a new pressure drop and deformation in the LC, leading to the formation of another cavity behind the new JT-GNP.

Although our study kept the spherical gold core at a fixed ~110 nm diameter, it is worthwhile considering how varying the core size might impact the LC defect topology and cavitation behavior. Generally, larger colloidal cores produce more extensive director distortions in nematic LCs, while smaller cores disturb the LC less.[47] In our Janus tadpole context, increasing the core diameter (with the same tail) would amplify the particle's overall elastic footprint and could make the topological defect structure more closely resemble that of a symmetric sphere (*i.e.*, stronger distortions centered on the sphere). Conversely, a much smaller core would accentuate the relative influence of the flexible tail, potentially leading to defect morphologies even more skewed or extended along the tail's axis. Nevertheless, the fundamental asymmetry-driven phenomena reported here would persist. Hydrodynamic cavitation remains governed by the presence of the flexible tail. A larger core could, in fact, enhance cavitation propensity by generating a larger low-pressure wake as the particle moves—analogous to a bigger obstacle in flow—while a smaller core might produce a weaker wake, making cavity nucleation more difficult under otherwise identical conditions. Notably, a symmetric spherical particle alone did not produce any cavities under our experimental conditions, underscoring the crucial role of tail-induced asymmetry. Therefore, core size modulates the magnitude and detail of the LC orientation field and cavitation threshold, but the emergence of irregular defect textures and air cavities remains intrinsically tied to the tadpole's asymmetry rather than the precise core diameter.[47]

Based on the same particle core size, the contrasting cavity behavior between long and short JT-GNP tails arises from their different impacts on the nematic director field and on flow-induced cavitation. A long flexible silica tail imposes a more extensive elastic distortion in the surrounding LC, especially under homeotropic anchoring where the tail's planar surface alignment conflicts with the bulk director orientation. This leads to higher elastic energy and more complex defect structures. For instance, the long tail can pull the particle's defect line outward into a branched ''butterfly'' shape that connects toward the cavity. Such an extended tail also perturbs a larger fluid volume as the particle moves, creating a pronounced low-pressure wake. In anisotropic fluids, even slow (Stokes-regime) flow past an object can produce a sudden pressure drop and cavitation.[34] Here, the long tail splits the LC flow and locally lowers the pressure, allowing air to be drawn in and nucleating

a larger cavity. Under stronger homeotropic boundaries, the LC resists reorientation more strongly, so the tail's fluctuations induce an even greater pressure dip and elastic stress, yielding larger cavities as anchoring strength increases (*e.g.*, cavity diameters ~45–55 μm). Once formed, these large cavities expand until the capillary pressure pulling the LC–air interface closed is balanced by the persistent tail-driven pressure drop and the elastic forces of the distorted LC, reaching a stable cavity at equilibrium. In contrast, a short, stubby tail perturbs only a localized region of the nematic and cannot generate such broad distortions or sustained flow effects. Shorter tails produce sharp but very local density changes, nucleating only small to moderate cavities (~40–50 μm). The limited length means the short tail cannot store as much elastic energy or create an extended defect, and its director-field distortion remains closer to that of a nearly spherical colloid. Truly spherical particles (with no tail) produce no cavities under identical conditions, underscoring that tail-induced asymmetry is the key driver. Thus, the long tail's greater asymmetry and length lead to a larger elastic and hydrodynamic disturbance – manifesting as elaborate "butterfly" defect wings in the LC and a significant flow-induced pressure drop – which together promote the formation of much larger cavities. Meanwhile, short-tailed JT-GNPs behave more like symmetric particles, causing relatively smaller cavity changes and defect morphologies.

The unique defect morphologies and cavitation behavior of our tadpole–nematic system open avenues for several applications. In actuators, the asymmetry-driven "butterfly" defects could be harnessed to convert external stimuli into controlled microscale motion or force. For example, periodic extension and contraction of LC defects around an asymmetric particle can propel a colloid or induce directed flows, as shown in defect-propelled microswimmers.[45] In adaptive materials, the ability to tune defect structures and form transient cavities on demand enables composites that dynamically alter their properties. By modulating the internal LC topology (for instance, adjusting porosity or optical anisotropy *via* defect reconfiguration), one can create soft matter systems that adapt to external stimuli in real time. Furthermore, controlled cavity formation and collapse could provide an "on-demand" mechanism for drug delivery since cavitation can overcome transport barriers in biological tissues.[48] Notably, although liquid-crystalline matrices are already studied as stimuli-responsive drug carriers,[36] the size of the tunable cavity in our system is several orders of magnitude larger than the original particle core size, providing the potential to store and release great amounts of therapeutic cargo at target sites. Integrating these features, future LC-based devices could serve as microactuators, adaptive metamaterials, or smart delivery vehicles that capitalize on defect engineering for advanced functionality.

Conclusion

In conclusion, based on synthetic Janus tadpole-shaped nanoparticles with gold cores and flexible silica tails of adjustable lengths, we introduced controllable asymmetry into the LC-particle system, which allowed for a nuanced study of the resulting director field distortions and defect morphologies. Experimental studies were performed in nematic 5CB LC cells, prepared under different surface anchoring conditions, to investigate the defect structures induced by the tadpole-shaped particles. These conditions led to the emergence of diverse defect morphologies, including distinct butterfly-like configurations, influenced by both tail length and the surface anchoring of the LC cell. Fluorescence microscopy studies were conducted to evaluate the softness and flexibility of the silica tails. Notably, this was the first time we developed a system capable of generating cavities and studying a new mechanism of cavity formation in anisotropic liquids, driven by hydrodynamic cavitation induced by tail fluctuations during particle movement. This mechanism involved localized perturbations caused by the asymmetry of the flexible silica tail, which led to a sudden pressure drop and the subsequent formation of cavities in the surrounding nematic LC. Numerical simulations were conducted to analyze the director field distortions around the JT-GNPs, showing that the director field differed when the JT-GNP was at different distances from the cavity. Overall, our findings show that introducing tadpole-shaped particles into nematic LCs enables the generation and control of irregular topological defects. The geometric asymmetry and flexibility of these particles offer insights into defect morphologies and interactions, with potential applications in soft robotics, adaptive materials, and directed self-assembly.

Experimental

Chemical and materials

Tetrachloroauric acid trihydrate ($HAuCl_4 \cdot 3H_2O$, ≥99.9%), 2-propanol anhydrous, 4-mercaptophenylacetic acid (4-MPAA, 97%), poly(acrylic acid) (average M_w = 1800) (PAA_{18}), and tetraethyl orthosilicate (TEOS) (99.9%) were purchased from Sigma-Aldrich. Sodium citrate dihydrate (99.0–101.0%) was purchased from Fischer Scientific, ethanol was purchased from Pharmco, ammonium hydroxide was purchased from Macron Fine Chemicals. Nanopure water with a resistivity of 18 MΩ cm was used in all experiments. All chemicals were used as received without further purification. 5CB is purchased from Grand Winton Inc. Octadecyl–trichlorosilane (OTS) was purchased from Sigma-Aldrich. PMMAZO, poly(6-(4-methoxy-azobenzene-4′-oxy) hexyl methacrylate), was obtained using the process reported by Stewart and Imrie.[49] Fluorescein isothiocyanate (FITC, 98.00%) was purchased from APExBIO. (3-Aminopropyl) trimethoxysilane (APTMS, 97%) was purchased from Sigma-Aldrich.

Solution preparation

Initially, 50 μL of 5CB was subjected to controlled heating to reach its isotropic phase at 40 °C, effectively enhancing its solubility. Following this, a precise mixture was created by combining 35 μL of nanoparticles with the 5CB solution. The resulting blend was then allowed to stand undisturbed for a

duration of 72 hours, facilitating the gradual evaporation of ethanol.

Surface modification

All silicon wafers and glass slides undergo a piranha treatment by immersion in solution made up of a 3 : 1 ratio of sulfuric acid and hydrogen peroxide for 1 hour held at 130 °C. The wafer was followed by rinsing with deionized water (DI) water at least three times to remove any residue. To produce the homeotropic anchoring, glass slides are soaked in 13.8 μL OTS and 120 mL Heptane solution for one hour followed by a dichloromethane rinse performed twice and dried with nitrogen air. PMMAZO treatment involved 0.05% PMMAZO in chlorobenzene spin coated onto a silicon wafer. The wafer is then transferred into a nitrogen chamber where it is baked for 5 min at 250 °C.

Cell construction

Silicon wafers and glass slides are cut and cleaned with nitrogen air. The Mylar thin film was used as a spacer to create a uniform 1.5 μm gap for the LC solution. To create the Planar cell, only the piranha treated silicon wafer and glass slide is used. For the Hybrid cell, piranha treated silicon wafer is the base and OTS treated glass is the top layer. The PMMAZO cell was made up of the PMMAZO silicon wafer and an OTS treated glass slide. All cells were held together with epoxy glue. Sonication forcefully disperses the particles, forming bubbles that implode, releasing energy into the solution and mitigating particle aggregation. The solution was then followed by sonication for 90 min. To better disperse the particles in 5CB, the solution was heated to 40 °C and vortexed for 5 minutes and repeated 3 times. The solution was again heated to 40 °C and about 3.5 μL of solution was injected into the cell and was filled by capillary effect.

Preparation of FITC conjugated JT-GNPs

JT-GNPs were first functionalized with APTMS which renders NH_2 groups on the silica surface. Typically, 2.5 mL of a JT-GNP ethanol solution mixed with 0.5 mL of APTMS was stirred for 24 hours in an 80 °C oil bath and subsequently cooled to room temperature until the reaction was complete. The JT-GNP solution was then washed twice with ethanol and eventually redispersed into 1 mL of nanopure water. The resulted APTMS modified JT-GNPs were further characterized and confirmed by measuring the zeta potential with a Malvern Panalytical Zetasizer Ultra DLS (Fig. S4). To synthesize a FITC conjugated silica shell, 1 mL of APTMS modified JT-GNP solution was mixed with 1 mg mL^{-1} solution of FITC to react overnight in a dark area. The resulted solution was washed *via* centrifuging four times using ethanol and the final precipitate was redispersed into 1 mL ethanol for further use.

Numerical methods

For the numerical experiments presented in the text we have considered a **Q**-tensor formulation to represent the orientation of the molecules.[50] The dynamics of the molecules was obtained by neglecting the hydrodynamics effects of the system and minimizing the Landau–de Gennes free energy functional (E_{LdG}) using a gradient flow:

$$\mathbf{Q}_t + \gamma\left(\frac{\delta E_{\mathrm{LdG}}}{\delta \mathbf{Q}}\right) = \mathbf{0},$$

with γ being a relaxation time parameter and $\frac{\delta E_{\mathrm{LdG}}}{\delta \mathbf{Q}}$ denoting the variational derivative of the free energy with respect to **Q**. In particular we have considered the one-constant form of the free energy:

$$E_{\mathrm{LdG}}(\mathbf{Q}) = \int_{\Omega}\left(\frac{1}{2}|\nabla \mathbf{Q}|^2 + \frac{1}{\varepsilon_{\mathbf{Q}}}\Psi(\mathbf{Q})\right)\mathrm{d}\boldsymbol{x}, \tag{1}$$

where $\frac{1}{2}|\nabla \mathbf{Q}|^2$ denotes the elastic energy density, $\Psi(\mathbf{Q})$ denotes the bulk energy density and $\varepsilon_{\mathbf{Q}} > 0$ is a dimensionless parameter that balances both energetic contributions. The one constant version of the original Landau–de Gennes elastic energy has proved useful to represent the dynamics of the molecules of nematic liquid crystals.[49,51–53] In particular, the bulk energy functional is denoted by a quartic polynomial in **Q**:

$$\Psi(\mathbf{Q}) = \frac{A}{2}\mathrm{tr}(\mathbf{Q}^2) - \frac{B}{3}\mathrm{tr}(\mathbf{Q}^3) + \frac{C}{4}\mathrm{tr}(\mathbf{Q}^2)^2 \tag{2}$$

Here B, $C > 0$ are material-dependent bulk constants, independent of the temperature, whereas the parameter A depends linearly on temperature,[54] that we assume is constant in our simulations. In our case, we consider $A = -0.2$ and $B = C = 1.0$.

The numerical simulations were performed using the ideas presented in ref. 55, where several accurate and efficient numerical schemes are proposed. In particular, we consider a semi-implicit finite difference numerical scheme in time and a conforming Finite Element discretization in space.

In all simulations, the considered domain is a rectangle where a circular shape has been removed from the domain as well as the shape of the tadpole (which has been represented by the union of a rectangle and a circle). In our case, we consider the same values of the parameters that have been considered in other theoretical studies previously performed using this model.[49,52] The rectangular domain has size $[0, 1.5] \times [0, 0.5]$, the bulk energy functional parameters are set to $A = -0.2$ and $B = C = 1.0$, the relaxation time is set to $\gamma = 1$ and the dimensionless parameter is set to $\varepsilon_{\mathbf{Q}} = 0.01$. Finally, the spatial discretization parameter is set to $\Delta x = 1/150$, the temporal discretization parameter is set to $\Delta t = 10^{-5}$, and the final time for the presented numerical results is $T = 0.1$.

The boundary conditions on the top and bottom boundary of the rectangular domain were set to homeotropic by imposing Dirichlet boundary conditions, while the lateral sides were considered in such a way that the molecules were free to arrange in any direction by imposing Neumann boundary conditions. Moreover, by using Dirichlet boundary conditions the configuration of the molecules in the big circle were set as homeotropic and the molecules associated with the tadpole shape were designed such that they were oriented parallel to its boundary.

Characterization techniques

All UV-vis spectra were obtained with the Agilent Cary 3500 UV-vis Spectrophotometer. The scanning transmission electron microscopy (STEM) images of silica coated gold particles were obtained using a JEOL-7200F field emission SEM operated at 30 kV.

Images of CLC cells were obtained by polarization microscopy (BX53 Olympus). Periods of striped pattern and the sizes of fingerprint domains were measured by the image processing program (ImageJ). PMMAZO film thicknesses were measured by an alpha-SE ellipsometer. Contact angles of the modified wafers were measured by a Dataphysics measuring device. Compensator angles were measured by a U-CTB Berek compensator (Olympus). The zeta potential of the APTMS modified JT-GNPs was measured using a Malvern Panalytical Zetasizer Ultra DLS.

The fluorescence images and videos were acquired with a Leica Stellaris 8 laser-scanning fluorescent confocal microscope. The JT-GNPs were located in a sandwich structure and were constructed by two glass slides and the particles were suspended in a clear nail polish solution. The TJ-GNPs were excited with 495 nm and 587 nm of white light lasers (WLL), and emission was detected using 500–581 nm and 592–750 nm bandpass filters.

Author contributions

X. L. and Y. B. conceived and designed the experiments. X. W., T. H., S. H., J. E. D. and T. Y. performed the experiments. G. T. conceived, designed, and performed the simulations. X. W, T. H., Y. B., G. T. and X. L. wrote the manuscript. X. L. and Y. B. guided the work. All authors discussed the results and contributed to data analysis and manuscript revision.

Conflicts of interest

There are no conflicts to declare.

Data availability

The data supporting the findings of this study have been included in the article and its SI. Other datasets generated during this study, such as raw and processed data, are available from the corresponding author upon reasonable request.

All supporting data are provided in the supplementary information, which contains synthesis details, microscopy images, zeta potential measurements, and videos of JT-GNP motion and cavity formation. See DOI: **https://doi.org/10.1039/d5ma00550g**.

Acknowledgements

This research was supported by the National Science Foundation award CBET-2344489. Teagan Hamlett also thanks the partial funding support from National Science Foundation award CHE-2108842. The fluorescence data acquisition on the Leica Stellaris 8 laser-scanning fluorescent confocal microscope was made possible through an NSF-MRI award (award no. 2019228). The Zeta potential data acquisition on the Malvern Panalytical Zetasizer Ultra DLS as made possible through an NSF-MRI award (award no. 2216466). STEM studies were conducted on an instrument funded by the Joint Center for Deployment and Research in Earth Abundant Materials (JCDREAM). The authors thank Michael Kraft, Alyssa Tsukada and Kyle Mikkelsen from the Advanced Materials Science & Engineering Center (AMSEC) and Scientific Technical Services (STS) at Western Washington University for their technical support on nanoparticle characterizations.

References

1 V. Vaibhav, A. Bera, A. C. Y. Liu, M. Baggioli, P. Keim and A. Zaccone, *Nat. Commun.*, 2025, **16**, 55.
2 M. J. Bowick, L. Chandar, E. A. Schiff and A. M. Srivastava, *Science*, 1994, **263**, 943–945.
3 L. Tubiana, G. P. Alexander, A. Barbensi, D. Buck, J. H. E. Cartwright, M. Chwastyk, M. Cieplak, I. Coluzza, S. Čopar, D. J. Craik, M. Di Stefano, R. Everaers, P. F. N. Faísca, F. Ferrari, A. Giacometti, D. Goundaroulis, E. Haglund, Y.-M. Hou, N. Ilieva, S. E. Jackson, A. Japaridze, N. Kaplan, A. R. Klotz, H. Li, C. N. Likos, E. Locatelli, T. López-León, T. Machon, C. Micheletti, D. Michieletto, A. Niemi, W. Niemyska, S. Niewieczerzal, F. Nitti, E. Orlandini, S. Pasquali, A. P. Perlinska, R. Podgornik, R. Potestio, N. M. Pugno, M. Ravnik, R. Ricca, C. M. Rohwer, A. Rosa, J. Smrek, A. Souslov, A. Stasiak, D. Steer, J. Sułkowska, P. Sułkowski, D. W. L. Sumners, C. Svaneborg, P. Szymczak, T. Tarenzi, R. Travasso, P. Virnau, D. Vlassopoulos, P. Ziherl and S. Žumer, *Phys. Rep.*, 2024, **1075**, 1–137.
4 S.-B. Wu, J.-B. Wu, H.-M. Cao, Y.-Q. Lu and W. Hu, *Phys. Rev. Lett.*, 2023, **130**, 78101.
5 A. Piccardi, A. Alberucci, N. Kravets, O. Buchnev and G. Assanto, *Nat. Commun.*, 2014, **5**, 5533.
6 P. Guillamat, J. Ignés-Mullol and F. Sagués, *Proc. Natl. Acad. Sci. U. S. A.*, 2016, **113**, 5498–5502.
7 G. Mirri, V. S. R. Jampani, G. Cordoyiannis, P. Umek, P. H. J. Kouwer and I. Muševič, *Soft Matter*, 2014, **10**, 5797–5803.
8 M. Mitov, *Chem. Phys. Chem.*, 2014, **15**, 1245–1250.
9 L. C. Head, Y. A. G. Fosado, D. Marenduzzo and T. N. Shendruk, *Soft Matter*, 2024, **20**, 7157–7173.
10 Y. Zushi, C. D. Schimming and K. A. Takeuchi, *Phys. Rev. Res.*, 2024, **6**, 23284.
11 H. Miyazako and T. Sakajo, *Proc. R. Soc. A*, 2024, **480**, 20230879.
12 D. Luo, J. Wu, Z. Guo, J. Xia and W. Hu, *Giant*, 2024, **20**, 100327.
13 H. Stark, *Phys. Rep.*, 2001, **351**, 387–474.
14 T. C. Lubensky, D. Pettey, N. Currier and H. Stark, *Phys. Rev. E: Stat. Phys., Plasmas, Fluids, Relat. Interdiscip. Top.*, 1998, **57**, 610–625.
15 O. D. Lavrentovich, *Liq. Cryst.*, 1998, **24**, 117–126.

16 P. Poulin, H. Stark, T. C. Lubensky and D. A. Weitz, *Science*, 1997, **275**, 1770–1773.
17 R. Wittmann, L. B. G. Cortes, H. Löwen and D. G. A. L. Aarts, *Nat. Commun.*, 2021, **12**, 623.
18 T. Araki and H. Tanaka, *Phys. Rev. Lett.*, 2006, **97**, 127801.
19 G. P. Alexander, B. G. Chen, E. A. Matsumoto and R. D. Kamien, *Rev. Mod. Phys.*, 2012, **84**, 497–514.
20 B. Fleury, B. Senyuk, M. Tasinkevych and I. I. Smalyukh, *Nano Lett.*, 2020, **20**, 7835–7843.
21 Y. Yuan, Q. Liu, B. Senyuk and I. I. Smalyukh, *Nature*, 2019, **570**, 214–218.
22 J. M. Ilnytskyi, A. Trokhymchuk and M. Schoen, *J. Chem. Phys.*, 2014, **141**, 114903.
23 S. Fumeron and B. Berche, *Eur. Phys. J.-Spec. Top.*, 2023, **232**, 1813–1833.
24 B. Behdani, J. Lumpkins and C. A. Silvera Batista, *Langmuir*, 2023, **39**, 9025–9034.
25 V. S. Devika, D. K. Sahu, R. K. Pujala and S. Dhara, *Phys. Rev. Appl.*, 2022, **18**, 14030.
26 S. Zhou, O. Tovkach, D. Golovaty, A. Sokolov, I. S. Aranson and O. D. Lavrentovich, *New J. Phys.*, 2017, **19**, 055006.
27 J. Invik, H. W. Barkema, A. Massolo, N. F. Neumann and S. Checkley, *J. Water Health*, 2017, **15**, 729–740.
28 J. Schwarz-Linek, J. Arlt, A. Jepson, A. Dawson, T. Vissers, D. Miroli, T. Pilizota, V. A. Martinez and W. C. K. Poon, *Colloids Surf., B*, 2016, **137**, 2–16.
29 S. Anand, X. Ma, S. Guo, S. Martiniani and X. Cheng, *Proc. Natl. Acad. Sci. U. S. A.*, 2024, **121**, e2411608121.
30 M. S. Karthikesh and X. Yang, *Exp. Biol. Med.*, 2021, **246**, 758–770.
31 F. Chavrier, J. Y. Chapelon, A. Gelet and D. Cathignol, *J. Acoust. Soc. Am.*, 2000, **108**, 432–440.
32 J. Tu and A. C. H. Yu, *BME Front.*, 2025, **2022**, 9807347.
33 C. C. Church and V. A. Khokhlova, *J. Acoust. Soc. Am.*, 2007, **121**, 3057.
34 T. Stieger, H. Agha, M. Schoen, M. G. Mazza and A. Sengupta, *Nat. Commun.*, 2017, **8**, 15550.
35 V. Manjuladevi, R. Pratibha and N. V. Madhusudana, *Phys. Rev. Lett.*, 2002, **88**, 55701.
36 L.-L. Ma, C. Liu, S.-B. Wu, P. Chen, Q.-M. Chen, J.-X. Qian, S.-J. Ge, Y.-H. Wu, W. Hu and Y.-Q. Lu, *Sci. Adv.*, 2025, **7**, eabh3505.
37 X. Li, T. Yanagimachi, C. Bishop, C. Smith, M. Dolejsi, H. Xie, K. Kurihara and P. F. Nealey, *Soft Matter*, 2018, **14**, 7569–7577.
38 M.-C. Estévez, M. B. O'Donoghue, X. Chen and W. Tan, *Nano Res.*, 2009, **2**, 448–461.
39 T. T. Nguyen, H. N. Nguyen, T. H. L. Nghiem, X.-H. Do, T. T. To, T. X. P. Do, D. L. Do, H. G. Nguyen, H. M. Nguyen, N. D. Nguyen, M. Q. Luu, T. N. Nguyen, T. B. N. Nguyen, V. T. Nguyen, V. T. Pham, U. T. T. Than and T. M. N. Hoang, *Sci. Rep.*, 2024, **14**, 6969.
40 C. J. Moore, G. Giovannini, F. Kunc, A. J. Hall and V. Gubala, *J. Mater. Chem. B*, 2017, **5**, 5564–5572.
41 L. Yang, A. Raza, Y. Si, X. Mao, Y. Shang, B. Ding, J. Yu and S. S. Al-Deyab, *Nanoscale*, 2012, **4**, 6581–6587.
42 F. Zhao, X. Wang, B. Ding, J. Lin, J. Hu, Y. Si, J. Yu and G. Sun, *RSC Adv.*, 2011, **1**, 1482–1488.
43 X. Mao, Y. Si, Y. Chen, L. Yang, F. Zhao, B. Ding and J. Yu, *RSC Adv.*, 2012, **2**, 12216–12223.
44 J. R. Crockett, M. Wang, J. E. Doebler, T. Pawale, X. Li and Y. Bao, *Chem. Mater.*, 2022, **34**, 9282–9293.
45 T. Yao, Ž. Kos, Q. X. Zhang, Y. Luo, E. B. Steager, M. Ravnik and K. J. Stebe, *Sci. Adv.*, 2024, **8**, eabn8176.
46 T. Yao, Ž. Kos, Q. X. Zhang, Y. Luo, F. Serra, E. B. Steager, M. Ravnik and K. J. Stebe, *Adv. Funct. Mater.*, 2022, **32**, 2205546.
47 M. Škarabot, A. V. Ryzhkova and I. Muševič, *J. Mol. Liq.*, 2018, **267**, 384–389.
48 B. Helfield, S. Sirsi, J. Kwan and M. Gray, *Pharmaceutics*, 2023, **15**, 15092207.
49 D. Stewart and C. T. Imrie, *Polymer*, 1996, **37**, 3419–3425.
50 P. G. de Gennes and J. Prost, *The Physics of Liquid Crystal*, 1993, vol. 2.
51 J. M. Ball, *Mol. Cryst. Liq. Cryst.*, 2017, **647**, 1–27.
52 J. Zhao, X. Yang, Y. Gong and Q. Wang, *Comput. Methods Appl. Mech. Eng.*, 2017, **318**, 803–825.
53 J. P. Borthagaray and S. W. Walker, in *Handbook of Numerical Analysis*, eds. A. Bonito and R. H. Nochetto, 2021, vol. 22, Elsevier, pp. 313–382.
54 A. Majumdar, *Eur. J. Appl. Math.*, 2010, **21**, 181–203.
55 J. Swain and G. Tierra, *Comput. Methods Appl. Mech. Eng.*, 2024, **430**, 117190.